Nano Research

ISSN 1998-0124 CN 11-5974/O4
https://doi.org/10.26599/NR.2026.94908676

Research Article

Reticuloendothelial system blockade-assisted redirection of celastrol-loaded nanomedicine to glomeruli for treatment of mesangioproliferative glomerulonephritis

Jiali Fu[1,§], Yujia Wang[1,§], Anqi Zhang[1], Ting Li[1], Yan Yuan[1], Kejin Chen[1], Shanshan He[2], Lin Li[3], Shiqi Huang[4], Ling Guo[5], Xun Sun[1], Tao Gong[1], Ling Zhang[3,4], Qing Lin[1](✉), Zhirong Zhang[1]

[1] Key Laboratory of Drug Targeting and Drug Delivery System of the Education Ministry and Sichuan Province, Sichuan Engineering Laboratory for Plant-Sourced Drug and Sichuan Research Center for Drug Precision Industrial Technology, West China School of Pharmacy, Sichuan University, Chengdu 610041, China

[2] College of Pharmaceutical Sciences, Liangzhu Laboratory, Zhejiang University, Hangzhou 310058, China

[3] West China School of Public Health and West China Fourth Hospital, Sichuan University, Chengdu 610041, China

[4] College of Polymer Science and Engineering, Sichuan University, Chengdu 610065, China

[5] National Engineering Technology Research Center for Miao Medicine, Guizhou Engineering Technology Research Center for Processing and Preparation of Traditional Chinese Medicine and Ethnic Medicine, College of Pharmaceutical Sciences, Guizhou University of Traditional Chinese Medicine, Guiyang 550025, China

[§] Jiali Fu and Yujia Wang contributed equally to this work.

Nano Res., **Just Accepted Manuscript** • https://doi.org/10.26599/NR.2026.94908676

https://www.sciopen.com/journal/1998-0124 on Mar. 25, 2026

Just Accepted

Insert Table of Contents artwork here

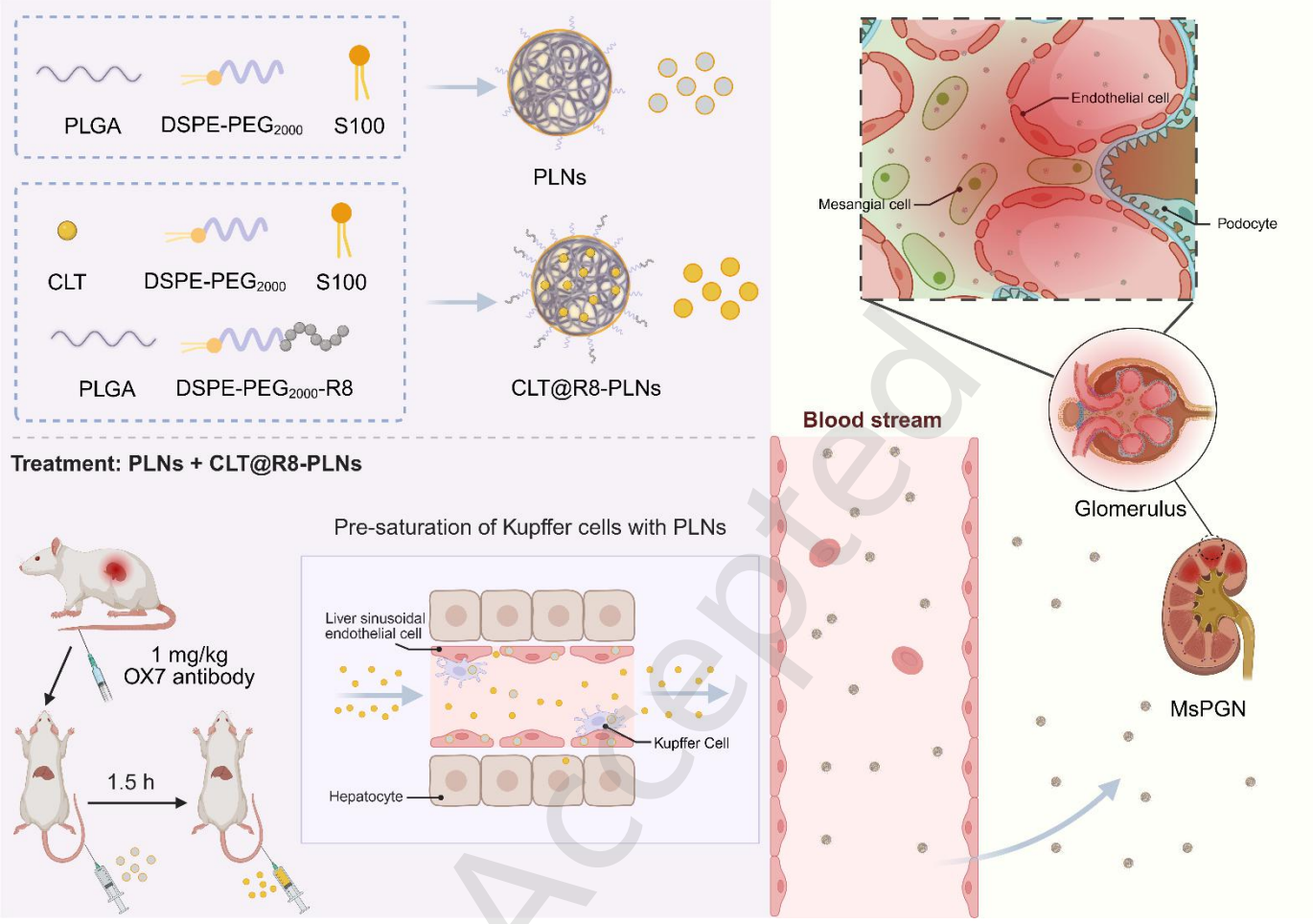

Schematic illustration of CLT@R8-PLNs preparation and RES blockade-assisted targeting to injured glomeruli for MsPGN treatment. Created in https://BioRender.com.

Research Article

Reticuloendothelial system blockade-assisted redirection of celastrol-loaded nanomedicine to glomeruli for treatment of mesangioproliferative glomerulonephritis.

Jiali Fu[1,§], Yujia Wang[1,§], Anqi Zhang[1], Ting Li[1], Yan Yuan[1], Kejin Chen[1], Shanshan He[2], Lin Li[3], Shiqi Huang[4], Ling Guo[5], Xun Sun[1], Tao Gong[1], Ling Zhang[3,4], Qing Lin[1] ✉, and Zhirong Zhang[1]

[1] *Key Laboratory of Drug Targeting and Drug Delivery System of the Education Ministry and Sichuan Province, Sichuan Engineering Laboratory for Plant-Sourced Drug and Sichuan Research Center for Drug Precision Industrial Technology, West China School of Pharmacy, Sichuan University, Chengdu 610041, China*

[2] *College of Pharmaceutical Sciences, Liangzhu Laboratory, Zhejiang University, Hangzhou 310058, China*

[3] *West China School of Public Health and West China Fourth Hospital, Sichuan University, Chengdu 610041, China*

[4] *College of Polymer Science and Engineering, Sichuan University, Chengdu 610065, China*

[5] *National Engineering Technology Research Center for Miao Medicine, Guizhou Engineering Technology Research Center for Processing and Preparation of Traditional Chinese Medicine and Ethnic Medicine, College of Pharmaceutical Sciences, Guizhou University of Traditional Chinese Medicine, Guiyang 550025, China*

[§] *Jiali Fu and Yujia Wang contributed equally to this work.*

Received: 24 February 2026; **Revised:** 24 March 2026; **Accepted:** 25 March 2026

✉ Address correspondence to qinglin@scu.edu.cn

Cite this article: *Nano Research*, 2026, 19, 94908676 https://doi.org/10.26599/NR.2026.94908676

ABSTRACT: Glomerulonephritis (GN), a major cause of chronic kidney disease, remains difficult to treat due to inefficient glomerular drug delivery following systemic administration. Here, we report a targeted nanotherapeutic strategy based on celastrol -loaded, positively charged poly(lactic-co-glycolic acid) nanoparticles (CLT@R8-PLNs) designed to promote glomerular accumulation. To further improve renal targeting, a reticuloendothelial system (RES) blockade strategy was employed by pre-saturating phagocytic organs with blank nanoparticles prior to CLT@R8-PLNs administration. *In vivo* biodistribution studies demonstrated that RES blockade markedly reduced hepatic and splenic sequestration while significantly enhanced glomerular accumulation of the nanoparticles. In a rat model of mesangioproliferative glomerulonephritis (MsPGN), this delivery strategy effectively alleviated glomerular inflammation and suppressed mesangial cell proliferation, accompanied by pronounced downregulation of monocyte chemoattractant protein-1, intercellular adhesion molecule-1, interleukin-6, interleukin-1β, and proliferating cell nuclear antigen. Collectively, these results demonstrate that integrating RES blockade with size-dependent passive targeting and charge-mediated glomerular interactions enables enhanced glomerular delivery and therapeutic efficacy, providing a rational nanomedicine-based approach for the treatment of GN.

KEYWORDS: reticuloendothelial system blockade, glomerular targeting, celastrol, mesangioproliferative glomerulonephritis

1 Introduction

Chronic kidney disease (CKD) is a leading cause of renal failure and end-stage renal disease (ESRD), accounting for approximately 45% of all existing ESRD cases worldwide [1]. Defined by persistent structural or functional abnormalities of the kidney lasting longer than three months [2], CKD affects more than 10% of the global population and imposes a substantial clinical and socioeconomic burden [3]. Among the diverse etiologies of CKD, glomerulonephritis (GN) represents a major category of immune-mediated renal disorders characterized by inflammatory injury to the glomeruli [4]. Mesangioproliferative glomerulonephritis (MsPGN) is one of the most prevalent and clinically significant subtypes of GN [3], featuring excessive mesangial cell proliferation and abnormal extracellular matrix deposition [5]. These pathological alterations promote the release of pro-inflammatory mediators, accelerate interstitial fibrosis, and ultimately drive progressive glomerulosclerosis and renal functional decline [6]. Therefore, therapeutic strategies capable of effectively suppressing glomerular inflammation and mesangial cell proliferation are critically important to delay or prevent progression to ESRD [7].

Current clinical management of MsPGN primarily relies on supportive care and non-specific immunosuppressive therapies [8, 9]. Although these approaches can partially alleviate symptoms, their therapeutic efficacy remains limited and is often accompanied by considerable systemic adverse effects [10]. A key challenge lies in the lack of effective strategies for selectively delivering therapeutics to inflamed glomeruli after systemic administration. Poor renal targeting leads to insufficient drug accumulation at disease sites, necessitating high systemic doses that exacerbate off-target toxicity. Consequently, the development of targeted drug delivery systems that enable precise glomerular

localization while minimizing systemic exposure represents a compelling and unmet clinical need.

Natural products have attracted increasing attention as therapeutic agents for inflammatory kidney diseases. Thunder God Vine (Tripterygium wilfordii Hook F.), a traditional Chinese medicinal herb, and its derivatives have been widely used in the treatment of renal disorders [11]. Celastrol (CLT), a major bioactive triterpenoid extracted from this plant, exhibits potent anti-inflammatory and immunomodulatory activities [12], and has demonstrated promising therapeutic effects in reducing proteinuria and improving glomerular function in experimental nephropathy [11, 13]. However, the clinical translation of CLT has been severely hampered by its narrow therapeutic window and dose-limiting systemic toxicities, including hepatotoxicity and neurotoxicity [14-16]. These limitations highlight the urgent need for delivery strategies that can preferentially concentrate CLT within diseased glomeruli while reducing off-target distribution.

Nanoparticle-based have emerged as powerful platforms for improving the pharmacokinetics, biodistribution, and therapeutic index of small-molecule drugs [17]. Among various nanocarriers, polylactic-co-glycolic acid (PLGA) has been extensively investigated owing to its biodegradability, biocompatibility, and flexible control over drug release profiles [18 19]. Importantly, nanoparticle size is a critical determinant of renal accumulation. The glomerulus, a specialized capillary tuft responsible for blood filtration and primary urine formation, is composed of fenestrated endothelial cells, the glomerular basement membrane, podocytes, and the mesangial matrix [20]. The first three components together constitute the glomerular filtration barrier, which effectively restricts the passage of nanoparticles larger than ~10 nm. In contrast, the mesangium, located between the glomerular capillary loops and composed of mesangial cells and mesangial matrix, is directly accessible through the endothelial fenestrations, which have pore sizes of approximately 80-150 nm [21]. Consequently, nanoparticles within the size range of 10-150 nm can traverse the fenestrated endothelium and preferentially access the mesangial compartment. Moreover, the inflamed glomerular microenvironment is characterized by increased negative charge density, which provides an opportunity for electrostatically mediated targeting [11, 22].

Cell-penetrating peptides (CPPs) offer an effective strategy to further enhance cellular uptake and tissue penetration of nanocarriers [23]. Octaarginine (R8), a cationic CPP composed of eight arginine residues, exhibits strong electrostatic interactions with negatively charged cell membranes and has been widely employed to promote intracellular delivery of nanomedicines [24]. Surface modification with R8 has been shown to significantly enhance cellular internalization and therapeutic efficacy in various disease models [25-27]. Given the negatively charged pathological milieu of inflamed renal tissues [20]. R8-functionalized nanoparticles are expected to exhibit improved glomerular and mesangial cell uptake.

Despite these advances, a major bottleneck for systemically administered nanomedicines remains inefficient biodistribution. It has been reported that only approximately 0.7% of intravenously injected nanoparticles ultimately accumulate at target sites [28], largely due to rapid opsonization and clearance by the reticuloendothelial system (RES) [29-31]. To address this issue, a RES blockade strategy has been proposed, whereby pre-administration of blank nanoparticles saturates phagocytic organs and delays the clearance of subsequently therapeutic injected nanoparticles [30, 32, 33]. Previous studies have demonstrated that nanoparticles with sizes exceeding 200 nm are particularly effective in achieving RES saturation, and that an optimal interval of approximately 1.5 h between the blocking dose and therapeutic administration can maximize circulation time and target accumulation [32, 34]. While this strategy has shown promise in oncology and inflammatory disease models, its potential to enhance renal-targeted nanotherapy remains largely unexplored.

In this study, we developed a targeted nanotherapeutic system composed of CLT-loaded PLGA nanoparticles surface-modified with the cell-penetrating peptide R8 (CLT@R8-PLNs) using a nanoprecipitation-based self-assembly method. The nanoparticles were engineered with a mean diameter of approximately 80 nm to facilitate passive glomerular accumulation, while surface-exposed R8 peptides were designed to promote cellular internalization. To further enhance renal targeting, a RES-blocking strategy was implemented by pre-injecting blank PLGA nanoparticles (~200 nm) 1.5 h prior to CLT@R8-PLNs administration. The biodistribution, targeting efficiency, and therapeutic efficacy of this delivery system were systematically evaluated *in vitro* and in a mesangioproliferative glomerulonephritis model *in vivo*. Our results demonstrate that combining size-dependent passive targeting with RES blockade markedly enhances glomerular accumulation of CLT@R8-PLNs, leading to effective suppression of inflammation and mesangial cell proliferation with improved safety. These findings highlight RES modulation as a rational and promising strategy for improving nanomedicine-based targeted therapy of glomerulonephritis.

2 Experimental

2.1 Materials, cells and animals

CLT (purity≥98%, Cas No. 34157-83-0) was purchased from Chengdu Manstar Biotechnology Co., Ltd. (Chengdu, China). PLGA (purity≥95%) was acquired from Chongqing Yu Mustache Pharmaceutical Technology Co., Ltd. (Chongqing, China). The cysteine-modified octaarginine peptide (Cys-R8, purity≥98%) was supplied by GL Biochem (Shanghai) Ltd. Soy lecithin (S100) was purchased from Liaoning Tieling Beiya Medicinal Oil Co., Ltd. (Tieling, China). 1,2-Distearoyl-sn-glycero-3-phosphoethanolamine-N-[methoxy(polyethylene glycol)-2000] (DSPE-PEG2000, purity≥95%) was supplied by Laysan Bio, Inc. (Arabia Mountain, USA). Dimethyl sulfoxide (DMSO) was purchased from Amresco Inc. (Solon, USA). The near-infrared fluorescent probe 1,1'-Dioctadecyl-3,3,3',3'-tetramethylindodicarbocyanine,4-chlorobenzenesulfonate salt (DiD, purity≥95%) was obtained from Biotium Inc. (Fremont, USA). In VivoMAb anti-mouse Thy1.1 (Cat No. BE0214) was purchased from Bio X Cell (Lebanon, USA). All other solvents and reagents were of analytical grade.

The rat glomerular mesangial cell line HBZY-1 was obtained from Wuhan Punosai Life Science and Technology Co., Ltd. (Wuhan, China). Cells were cultured in high-glucose Dulbecco's Modified Eagle Medium (DMEM; Gibco, New York, USA) supplemented with 10% (v/v) fetal bovine serum (FBS; Gibco, New York, USA) and 1% penicillin-streptomycin (HyClone, Logan, USA) at 37 °C in a humidified atmosphere containing 5% CO2.

Male Sprague-Dawley (SD) rats (5-6 weeks old, 200 ± 20 g) were purchased from Dossy Experimental Animal Co., Ltd. (Chengdu, China). All animal experiments were performed in accordance with guidelines for the care and use of laboratory animals and were approved by the Animal Ethics Committee of Sichuan University (Approval No. KS2020022, Chengdu, China).

2.2 Preparation and characterizations of CLT@R8-PLNs

CLT@R8-PLNs were prepared using a self-assembly nanoprecipitation method [35]. Briefly, CLT (12 mg), PLGA (20 mg), DSPE-PEG2000 (6 mg), DSPE-PEG2000-R8 (2 mg), and S100 (4 mg) were dissolved in 2 mL of DMSO to form the organic phase. The resulting solution was added dropwise into 4 mL of deionized water under stirring at room temperature. After addition, the dispersion was stirred continuously for 30 min to allow nanoparticle self-assembly. The resulting nanoparticles were subsequently dialyzed against deionized water for 24 h to remove residual organic solvent. PLGA nanoparticles with diameter of ~200 nm were prepared using the same formulation composition and procedure as the drug-loaded nanoparticles. To obtain particles with a larger mean diameter suitable for RES blockade, the total formulation amount was increased fivefold while maintaining the same component ratios.

The hydrodynamic diameter, polydispersity index (PDI), and zeta potential of the nanoparticles were determined by dynamic light scattering (DLS; Zetasizer Nano ZS90, Malvern Instruments, Worcestershire, UK). Particle morphology was examined by transmission electron microscopy (TEM; Tecnai G2 F20 S-TWIN, FEI Company, Eindhoven, the Netherlands).

The encapsulation efficiency (EE%) and drug loading capacity (DL%) of CLT@R8-PLNs were quantified as follows. To separate unencapsulated CLT, a known volume of freshly prepared nanoparticle suspension was transferred into a dialysis bag (MWCO 3.5 kDa, YA1078, Solarbio, Beijing, China) and dialyzed exhaustively against deionized water. The amount of CLT retained within the dialyzed nanoparticles (We) was determined by high-performance liquid chromatography (HPLC; 1260, Agilent Technologies, Santa Clara, USA). The total amount of CLT in an equal volume of the formulation before dialysis (Wt) was measured after dissolving the nanoparticles in DMSO. Encapsulation efficiency was calculated: EE% = (We / Wt) × 100%. For drug loading determination, a known volume of purified CLT@R8-PLNs suspension was lyophilized to obtain the total mass of solid nanoparticles (Wd). Drug loading capacity was calculated: DL% = (We / Wd) × 100%.

The in vitro release profile of CLT from CLT@R8-PLNs was evaluated using a dynamic dialysis method, with free CLT solution and non-targeted CLT-loaded PLGA nanoparticles (CLT-PLNs) serving as controls. Samples were sealed in dialysis bags (MWCO 3.5 kDa) and immersed in 40 mL of release medium (0.01 M phosphate-buffered saline, PBS, pH 7.4, containing 0.2% Tween 80) in 50-mL centrifuge tubes. The tubes were incubated in a thermostatic shaker (HZQ-F160A， Shanghai Yiheng Scientific Instrument Co., Ltd, Shanghai, China) at 37 °C and 100 rpm. At predetermined time points, 1 mL of the external medium was withdrawn and replaced with an equal volume of fresh, pre-warmed release medium. The collected samples were mixed with a fourfold volume of methanol, vortexed, and analyzed by HPLC to determine cumulative CLT release.

To evaluate storage stability, freshly prepared CLT@R8-PLNs dispersions were sealed and stored at 4 °C. Changes in particle size and PDI were monitored over a period of one week.

2.3 *In vitro* cytotoxicity and cellular uptake of CLT@R8-PLNs

The *in vitro* cytotoxicity of CLT@R8-PLNs was evaluated by in HBZY-1 cells using a CCK-8 assay. Cells were seeded in 96-well plates at a density of 1.5×10^4 cells per well and cultured until approximately 50% confluence was reached. Cells were then treated with free CLT, CLT-PLNs, or CLT@R8-PLNs. To investigate the effect of nanoparticle pre-saturation, an *in vitro* RES-blocking group was included, in which cells were pre-incubated with blank PLGA nanoparticles (PLGA at 300 ng/mL) for 1.5 h prior to the addition of CLT@R8-PLNs. All formulations were tested over a CLT concentration range of 0.125, 0.25, 0.5, 1.0, 2.0, and 4.0 μg/mL, with six replicates per concentration. After 24 h of incubation, the culture medium was replaced with fresh medium containing 10% (*v/v*) CCK-8 reagent, followed by incubation for an additional 2 h. Absorbance was measured at 450 nm using a microplate reader (Varioskan LUX, Thermo Fisher Scientific, Waltham, MA, USA). Cell viability was calculated according to the following equation: $(OD_{sample} - OD_{blank}) / (OD_{control} - OD_{blank}) \times 100\%$. Cellular uptake of the nanoparticles was assessed in HBZY-1 cells using DiD as a model probe. DiD-labeled PLNs and R8-PLNs were prepared following the same procedure described in Section 2.2, with DiD substituting for CLT. Cells were seeded in 12-well plates at a density of 1.5×10^5 cells per well and allowed to adhere for 24 h. After washing with PBS, cells were incubated with nanoparticle formulations diluted in serum-free medium to a final DiD concentration of 300 ng/mL. The experimental groups included PLNs, R8-PLNs, and an *in vitro* RES-blocking group, in which cells were pre-incubated with blank nanoparticles (PLGA at 300 ng/mL) for 1.5 h prior to incubation with R8-PLNs. After incubation for 2 h at 37 °C, cells were washed thoroughly with PBS, detached using 0.25% trypsin-0.02% EDTA, collected by centrifugation, and washed three times with PBS. The cell pellets were finally resuspended in PBS and analyzed quantitatively by flow cytometry (FACSCelesta, BD Biosciences, San Jose, CA, USA).

To elucidate cellular internalization mechanisms of R8-PLNs, endocytic pathway inhibition studies were performed. HBZY-1 cells were seeded in 12-well plates at a density of 1.5×10^5 cells per well. Prior to the nanoparticle exposure, cells were pre-incubated for 1 h in serum- and antibiotic-free medium containing specific endocytosis inhibitors: sodium azide (NaN_3, 154 μM) to inhibit ATP-dependent processes; chlorpromazine (CPZ, 25 μM) to block clathrin-mediated endocytosis; dimethyl amiloride (DMA, 100 μM) to inhibit macropinocytosis; or nystatin (Nys, 25 μM) to inhibit caveolae-mediated endocytosis. A low-temperature group (4 °C) and a positive control group (37 °C, no inhibitor) were included for comparison. Following inhibitor pre-incubation, DiD-labeled R8-PLNs were added to each well at a final DiD concentration of 300 ng/mL and incubated for an additional

2 h. Cells were subsequently washed, harvested, and analyzed by flow cytometry to quantify nanoparticle uptake.

2.4 *In vivo* biodistribution and glomerular accumulation of CLT@R8-PLNs

The *in vivo* biodistribution of nanoparticles was investigated in healthy male SD rats using the near-infrared fluorescent probe DiD. DiD-labeled nanoparticles, including non-modified PLNs, R8-PLNs and blank PLGA nanoparticles with a mean diameter of approximately 200 nm for RES blockade, were prepared as described in Section 2.2.

To determine the optimal time point for renal accumulation analysis, a preliminary biodistribution kinetic study was first performed. Rats were intravenously injected via the tail vein with either R8-PLNs alone or R8-PLNs following RES pre-blockade. For RES blockade, blank PLGA nanoparticles were administered at a dose of 12.5 mg PLGA/kg body weight 1.5 h prior to the injection of DiD-labeled R8-PLNs. Whole-body fluorescence imaging was conducted at 5 min, 15 min, 30 min, 1 h, 2 h, 4 h, and 8 h post-injection using an i*n vivo* imaging system (IVIS Lumina III; PerkinElmer, Waltham, MA, USA). Based on the kinetic fluorescence profiles, 15 min post-injection was identified as the time point corresponding to peak renal fluorescence intensity and was therefore selected for subsequent comparative biodistribution studies.

For the comparative biodistribution experiment, rats were randomly divided into four groups (n = 5 per group) and intravenously administered one of the following formulations: free DiD, PLNs, R8-PLNs, or R8-PLNs with RES pre-blockade (using the same blank nanoparticle dosing and timing regimen). The DiD dose was standardized at 100 μg/kg for all DiD-containing formulations, while control animals received an equivalent volume of 0.9% saline. At 15 min post-injection, animals were euthanized, and the kidneys were immediately harvested, rinsed with PBS, and subjected to *ex vivo* fluorescence imaging under identical acquisition settings (excitation/emission: 498/520 nm). Fluorescence intensity in the kidneys was quantified using the corresponding IVIS analysis software.

To further assess the intrarenal distribution and glomerular accumulation of the nanoparticles, kidney tissues were processed for fluorescence microscopy. Following *ex vivo* imaging, excised kidneys were embedded in optimal cutting temperature (OCT) compound and rapidly frozen. Cryosections with a thickness of 6 μm were prepared using a cryostat and mounted onto glass slides. The sections were fixed with 4% paraformaldehyde for 10 min at 4 °C, rinsed with PBS, and sealed using an antifade mounting medium. Fluorescence images were acquired using an inverted fluorescence microscope to visualize and compare the localization of different formulations within the glomerular regions.

2.5 Therapeutic evaluation of CLT@R8-PLNs

The therapeutic efficacy of CLT@R8-PLNs was evaluated in a MsPGN rat model. Male SD rats (5-6 weeks old) were intravenously injected with a single dose of anti-Thy1.1 monoclonal antibody (1 mg/kg) on day 0 to induce a MsPGN model, as previously described [36]. Rats were randomly assigned into six groups (n = 5 per group): (1) Normal group (healthy rats receiving PBS); (2) PBS group (MsPGN rats receiving PBS); (3) Free CLT group; (4) CLT-PLNs group; (5) CLT@R8-PLNs group; and (6) RES group (MsPGN rats pretreated with blank nanoparticles, followed by CLT@R8-PLNs administration 1.5 h later). All treatment groups received intravenous injections at an equivalent CLT dose of 1 mg/kg on days 2, 3, and 4 after model establishment. On day 5, therapeutic efficacy was evaluated by assessing proteinuria, renal histopathology, and inflammatory marker expression.

Proteinuria was quantified to assess renal function. Rats were individually housed in metabolic cages for 24 h urine collection. Collected urine samples were centrifuged at 1000 g for 3 min to remove debris. The supernatant was collected, and total urinary protein concentration was determined using a bicinchoninic acid (BCA) protein assay kit (Solarbio, Beijing, China) according to the manufacturer's instructions.

For serum biochemical analysis, approximately 0.5 mL of orbital blood was collected from each rat placed into 1.5 mL EP tubes and allowed to stand at room temperature for 1 h to facilitate serum separation. Samples were then centrifuged at 4720 g for 5 min at 4 °C, and the supernatant serum was collected. Serum creatinine (Crea) and urea nitrogen (Urea) levels were measured using a fully automated biochemical analyzer (7020, Hitachi High-Technologies Corporation, Tokyo, Japan).

For histopathological evaluation, kidney tissues were fixed in 4% paraformaldehyde at room temperature for 48 h, followed by dehydration, paraffin embedding, and sectioning at a thickness of 4 μm. The sections were deparaffinized, rehydrated, and stained with hematoxylin and eosin (H&E) following standard protocols. Glomerular and tubular morphological changes were examined under a light microscope.

Immunohistochemical staining was performed to evaluate renal inflammation and mesangial cell proliferation. Paraffin-embedded kidney sections were stained for interleukin-6 (IL-6; 1:500, DF6087, Affinity Biosciences, Changzhou, China), interleukin-1β (IL-1β; 1:500, AF5103, Affinity Biosciences, Changzhou, China), and proliferating cell nuclear antigen (PCNA; 1:100, AF0239, Affinity BioSciences, Changzhou, China). After dewaxing and rehydration, antigen labeling and immunostaining were conducted according to standard immunohistochemical procedures. Hematoxylin was used for nuclear counterstaining, followed by differentiation and bluing. The sections were then dehydrated through graded ethanol, cleared in xylene, mounted with neutral resin, and examined under a light microscope.

The mRNA expression levels of inflammatory markers, including IL-6, IL-1β, monocyte chemoattractant protein-1 (MCP-1), and intercellular adhesion molecule-1 (ICAM-1), in renal cortical tissues were quantified by quantitative real-time PCR (qRT-PCR). Total RNA was extracted using the M5 Universal RNA Mini Kit (Mei5 Biotechnology, Beijing, China) and reverse-transcribed into cDNA using the TIANscript RT Kit (Tiangen, Beijing, China). qPCR was performed using SsoFast™ EvaGreen Supermix on an iCycler iQ™ 5 detection system (Bio-Rad, USA). Gene-specific primers (sequences listed in Supplementary Table S1) were synthesized by Sangon Biotech (Shanghai, China). Rat β-actin was used as the internal reference gene. Relative gene expression levels were calculated using the $2^{(-\Delta\Delta Ct)}$ method.

2.6 Preliminary safety evaluation of CLT@R8-PLNs treatment

A preliminary safety evaluation was conducted to assess the systemic biocompatibility of CLT@R8-PLNs following repeated intravenous administration. Healthy male SD rats were randomly divided into five groups (n = 5 per group): (1)

Normal group; (2) Free CLT group; (3) CLT-PLNs group; (5) CLT@R8-PLNs group; and (5) RES group (rats pretreated with blank nanoparticles followed by CLT@R8-PLNs administration). All formulations were administered via intravenous injection at an equivalent CLT dose of 1 mg/kg once daily for three consecutive days. Potential treatment-related toxicity was evaluated by analyzing serum biochemical parameters and histopathological changes in major organs.

Systemic biochemical profiling was performed to assess possible functional impairment of major organs. Serum samples were prepared as described in Section 2.5, were analyzed using the
fully automated biochemical analyzer. The following indicators were measured: renal function markers, including CREA and Urea; hepatic function markers, including alanine aminotransferase (ALT), aspartate aminotransferase (AST), and total protein (TP); and myocardial injury markers, including creatine kinase isoenzyme (CKMB) and lactate dehydrogenase (LDH).

Histopathological evaluations were subsequently conducted. After completion of the treatment regimen, rats were euthanized, and major organs, including the heart, liver, spleen, lungs, and kidneys, were carefully excised. The harvested tissues were rinsed with 0.9% saline and immediately fixed in 10% neutral buffered formalin (Solarbio, Beijing, China) for 48 h. Following fixation, the tissues were processed using standard paraffin-embedding procedures, sectioned, and stained with H&E according to established protocols [37]. Histopathological changes were examined under a light microscope.

2.7 Statistical Analysis

All data were expressed as mean ± standard deviation (SD). Statistical analyses were performed using GraphPad Prism 8 (GraphPad Software, USA). Comparisons between two groups were conducted using Student's t-test, while multiple group comparisons were analyzed using one-way analysis of variance followed by Tukey's post hoc test. A p-value of less than 0.05 was considered indicative of a statistically significant difference.

3 Results and discussion

3.1 Successful preparation and characterization of CLT@R8-PLNs

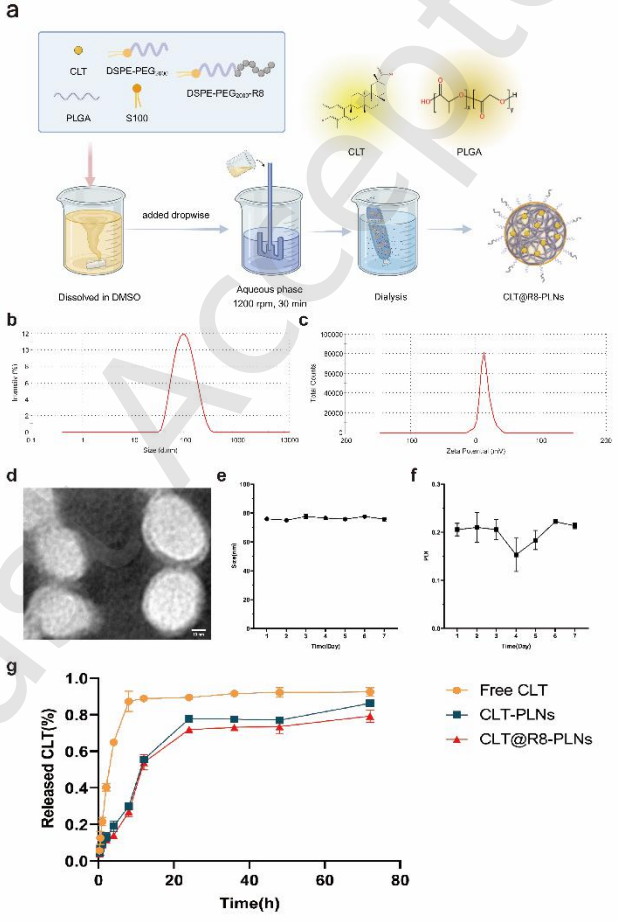

Fig. 1 | Preparation and characterization of CLT@R8-PLNs. (a) Schematic illustration of the preparation process of the CLT@R8-PLNs. Created with https://BioRender.com (b) Hydrodynamic size distribution of CLT@R8-PLNs measured by dynamic light scattering. (c) Zeta potential of CLT@R8-PLNs. (d) TEM image showing predominantly spherical morphology of CLT@R8-PLNs. Scale bar: 10 nm. (e, f) Stability of CLT@R8-PLNs over 7 days at 4 °C, showing minimal changes in particle size (E) and PDI (F). (G) In vitro drug release profiles of free CLT, CLT-PLNs, and CLT@R8-PLNs over 72 h. CLT-PLNs and CLT@R8-PLNs exhibited slower and more sustained release compared with free CLT.

Following systematic optimization of key formulation variables (Tables S1-S4), CLT@R8-PLNs were successfully fabricated using a self-assembly nanoprecipitation technique [35] (Figure 1a). The
optimized formulation consisted of CLT, PLGA, DSPE-PEG2000, DSPE-PEG2000-R8, and S100 at a mass ratio of 6:10:3:1:2. DLS analysis revealed that CLT@R8-PLNs possessed a narrow size distribution with a hydrodynamic diameter of 74.92 ± 0.94 nm and a polydispersity index (PDI) below 0.2, indicating high formulation homogeneity (Figure 1b, and Table S5). The nanoparticles carried a moderately positive surface charge, with a zeta potential of 13.63 ± 0.72

mV (Figure 1c, and Table S5), which is favorable for electrostatic interactions with the negatively charged membranes of glomerular cells and may facilitate cellular association and uptake.

TEM further confirmed that CLT@R8-PLNs were spherical, uniformly shaped, and well-dispersed, with no obvious aggregation observed (Figure 1d). The encapsulation efficiency and loading capacity, quantified by a combined dialysis with HPLC analysis, reached approximately 94.02% and 2.58 ± 0.04%, respectively (Table S6). Moreover, the resulting blank PLGA nanoparticles exhibited a mean diameter of 200.87 ± 2.64 nm with a PDI of 0.185 ± 0.025, confirming that the fivefold scale-up successfully maintained the desired particle size and homogeneity (Table S7). These results demonstrate the strong capability of the nanoprecipitation-based formulation to efficiently incorporate the hydrophobic drug CLT into the PLGA-based lipid–polymer hybrid nanoparticles.

Stability studies revealed that both particle size and zeta potential remained essentially unchanged over at least one week when of storage at 4 °C (Figure 1e and f), indicating good short-term colloidal stability suitable for subsequent biological evaluations. In vitro release studies showed that CLT@R8-PLNs exhibited a sustained release profile compared with the rapid release observed for free CLT (Figure 1g). Although no significant difference was detected between CLT-PLNs and CLT@R8-PLNs during the initial 18 h, CLT@R8-PLNs demonstrated a more controlled release behavior at later time points. This delayed release may be attributed to the surface R8 modification, which may influence diffusion pathways, alter polymer hydration kinetics, and/or affect drug-polymer interactions within the nanoparticle structure [38-40]. Collectively, these results indicate that CLT@R8-PLNs possess well-defined physicochemical properties, high drug-loading efficiency, favorable stability, and controlled release characteristics, providing a solid foundation for subsequent *in vivo* and *in vitro* investigations.

3.2 Enhanced cellular uptake and *in vitro* biocompatibility of CLT@R8-PLNs in glomerular mesangial cells

The cytotoxicity of different CLT formulations toward HBZY-1 cells was first evaluated to assess their *in vitro* biocompatibility. As shown in Figure 2a, both CLT-PLNs and CLT@R8-PLNs

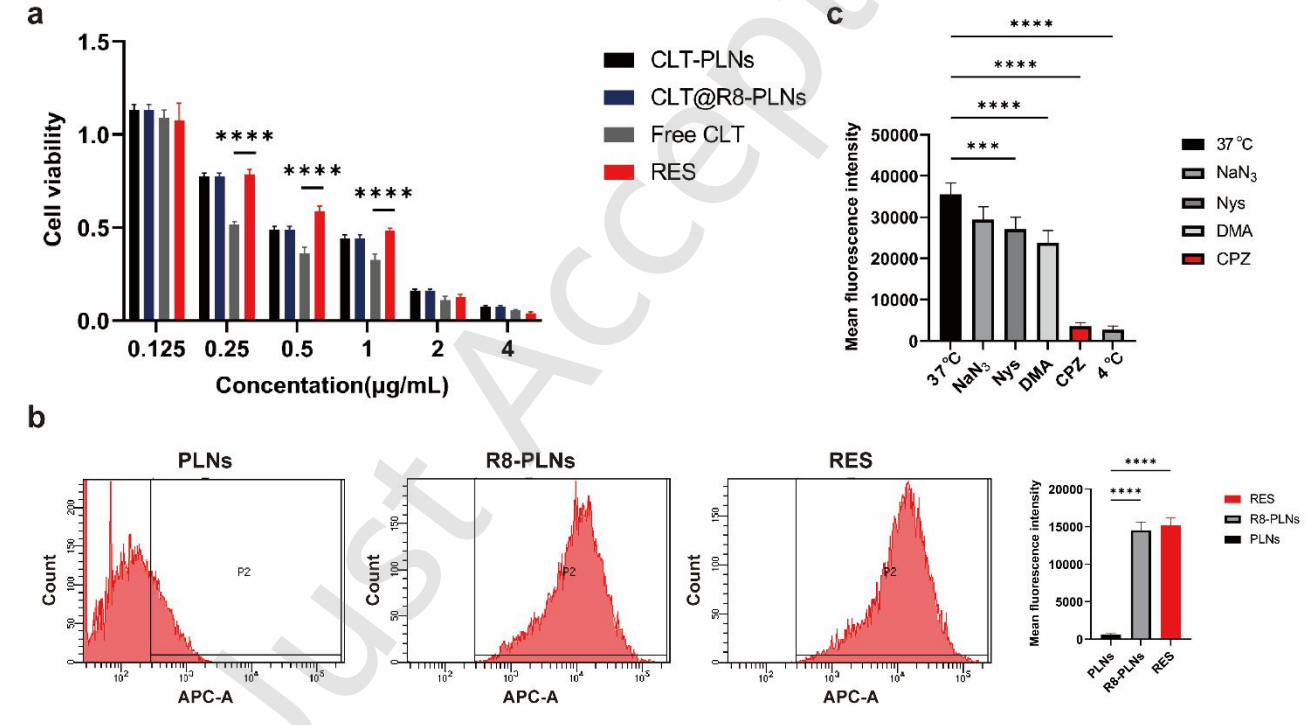

Fig. 2 | *In vitro* cytotoxicity and cellular uptake analysis of CLT@R8-PLNs. (A) Cell viability of HBZY-1 cells treated with free CLT, CLT-PLNs, CLT@R8-PLNs, and RES at concentrations of 0.125-4.0 μg/mL. The RES-blocking group exhibited reduced cytotoxicity and improved cell viability, indicating superior biocompatibility. (B) Cellular uptake of PLNs, R8-PLNs and RES in HBZY-1 cells. Flow cytometry analysis revealed that R8 modification significantly enhanced nanoparticle internalization compared with unmodified PLNs (**** $p < 0.0001$vs. PLNs). (C) Uptake of R8-PLNs under 4 °C and in the presence of endocytic inhibitors. Cellular internalization is energy-dependent and predominantly mediated via clathrin-mediated endocytosis. All data are presented as mean ± SD; *** $p < 0.001$, **** $p < 0.0001$, vs. 37 °C control.

exhibited significantly lower cytotoxicity compared with free CLT across the tested concentration range, indicating that nanoparticle encapsulation effectively mitigated the inherent cytotoxicity of CLT toward mesangial cells. Importantly, the RES-blocking group, which involved pre-incubation with blank nanoparticles, did not show additional cytotoxicity relative to the CLT@R8-PLNs group, suggesting that the introduction of blank nanoparticles did not compromise cellular safety. These findings support the suitability of the nanoparticle-based formulations for further cellular and *in vivo* experiments.

To determine whether R8 modification enhanced cellular internalization, the uptake efficiency of different formulations by HBZY-1 cells was quantitatively analyzed by flow cytometry. Results showed that R8-PLNs exhibited significantly higher cellular uptake than non-modified PLNs (Figure 2b), confirming that surface decoration with R8 markedly promoted nanoparticle internalization. This enhancement is likely attributable to the strong electrostatic interactions between the positively charged R8 residues and

the negatively charged cell membrane, facilitating membrane association and subsequent endocytosis.

Although the RES-blocking strategy is expected to enhance nanoparticle availability *in vivo*, no further increase in cellular uptake was observed in the RES-blocking group under *in vitro* conditions. This outcome is reasonable given the absence of an intact reticuloendothelial system in cell culture models. Notably, the presence of blank nanoparticles did not interfere with the uptake of R8-PLNs, indicating that the combined use of R8 modification and RES-blocking is mechanistically compatible rather than competitive.

To further elucidate the cellular internalization mechanisms of R8-PLNs, endocytosis inhibition studies were conducted. pre-treatment with nystatin (Nys, caveolae-mediated endocytosis inhibitor), dimethyl amiloride (DMA, macropinocytosis inhibitor), and chlorpromazine (CPZ, clathrin-mediated endocytosis inhibitor) all significantly reduced nanoparticle uptake, with chlorpromazine producing the most pronounced inhibitory effect (Figure 2c). These results indicate that the internalization of R8-PLNs by mesangial cells involves multiple pathways, including clathrin-mediated endocytosis and macropinocytosis, with clathrin-dependent uptake playing a dominant role. Moreover, the markedly reduced uptake observed at 4 °C and in the presence of sodium azide (NaN3) further confirmed that R8-PLN internalization is an active, energy-dependent process.

In summary, the *in vitro* cellular studies demonstrate that CLT@R8-PLNs exhibit good biocompatibility, significantly enhanced cellular uptake, and well-defined internalization mechanisms in mesangial cells. These findings validate the rational design of the R8-modified delivery system at the cellular level and provide strong support for its subsequent evaluation *in vivo*.

3.3 Specific renal and glomerular accumulation of CLT@R8-PLNs

To evaluate the *in vivo* fate and renal targeting behavior of the nanoparticles, DiD was employed as a near-infrared fluorescent tracer for real-time imaging [41]. Kinetic analysis revealed rapid renal accumulation of the nanoparticles as early as 5 min post-injection, with fluorescence intensity reaching a maximum at 15 min and gradually declining thereafter (Figure 3a). This temporal

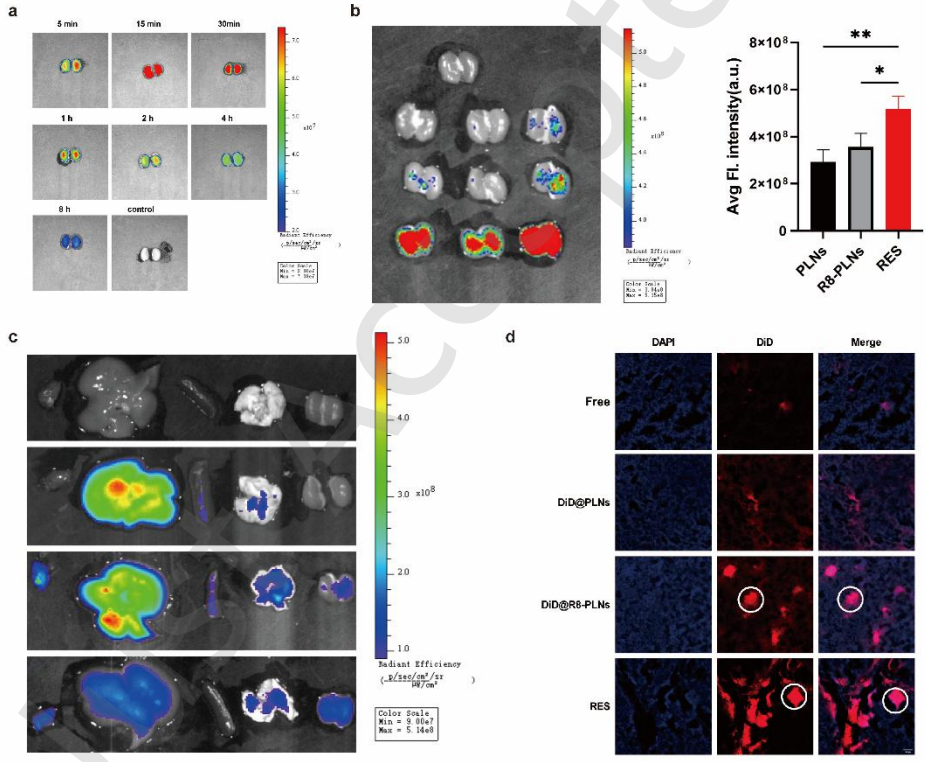

Fig. 3 | *In vivo* renal distribution and glomerular targeting under RES-blocking strategy. (a) Time-course of renal fluorescence intensity following injection of DiD-labeled nanoparticles. Fluorescence in the kidneys peaked at 15 min post-injection, which was selected for subsequent comparative analyses. (b) Quantitative comparison of renal fluorescence intensity at 15 min post-injection for different DiD-labeled formulations. The RES-blocking group exhibited the strongest renal signal, indicating enhanced nanoparticle accumulation. All data are presented as mean ± SD, *p < 0.05, ** p < 0.01 vs. RES group. (c) *Ex vivo* fluorescence imaging of major organs at 15 min post- injection. The RES- blocking group showed strongest fluorescence in the kidneys and weakest in the liver. (d) Representative confocal images of kidney sections at 15 min post- injection. RES blockade markedly enhanced fluorescence accumulation specifically within the glomeruli.

profile suggests a fast distribution phase followed by systemic clearance, and therefore the 15-min time point was selected for subsequent comparative biodistribution analysis.

At this optimal time point, *in vivo* fluorescence imaging demonstrated that renal signal intensity in the RES-blocking group was significantly higher than that observed in all other formulation groups (Figure 3b). *Ex vivo* imaging of excised organs further revealed a distinct distribution pattern: the RES-blocking group exhibited the strongest fluorescence signal in the kidney concomitant with the weakest in the liver (Figure 3c). Given that the liver represents the primary site of nanoparticle sequestration by the RES, this inverse liver–kidney signal relationship indicates that RES pre-saturation effectively reduced non-specific hepatic uptake and prolonged systemic availability of CLT@R8-PLNs [42, 43]. As a result, a greater fraction of the administered CLT@R8-PLNs was redirected toward the renal compartment.

To further delineate intrarenal localization, kidney

cryosections were examined by fluorescence microscopy. Nanoparticles in the RES-blocking group displayed markedly enhanced fluorescence specifically within the glomeruli compared with all other groups (Figure 3d). While the current imaging resolution does not allow precise discrimination of intra-glomerular cell-type localization, the observed fluorescence signal is consistent with mesangial retention. The ~80 nm size of CLT@R8-PLNs enables passage through the fenestrated glomerular endothelium (80-150 nm) while restricting further filtration across the glomerular basement membrane, leading to physical retention within the mesangial compartment [21]. Moreover, the cationic surface conferred by R8 may facilitate electrostatic interactions with the negatively charged mesangial matrix, further promoting mesangial localization. Importantly, RES blockade primarily enhances the number of nanoparticles reaching the glomeruli without altering this size- and charge-dependent intra-glomerular distribution. This observation suggests that RES blockade not only increases overall renal exposure but also promotes effective delivery of R8-PLNs to the primary pathological site in MsPGN. Importantly, RES blockade did not uniformly increase nanoparticle accumulation across all organs; rather, it selectively reduced hepatic and splenic uptake while preferentially enhancing renal, particularly glomerular, deposition. This pattern indicates a redirection of biodistribution rather than a mere extension of circulation time.

Collectively, these findings demonstrate that the integration of RES pre-saturation and R8-mediated cellular affinity enables both enhanced renal accumulation and preferential glomerular localization. This dual strategy establishes a favorable pharmacokinetic and biodistribution profile, providing a solid basis for the subsequent therapeutic efficacy of CLT@R8-PLNs.

3.4 Improved therapeutic efficacy of CLT@R8-PLNs in the MsPGN rat model

A rat model of MsPGN was established by intravenous administration of an anti-Thy1.1 monoclonal antibody (OX-7), as previously reported [36, 44]. The anti-Thy1.1 model exhibits a well- defined time-dependent disease progression. Mesangiolysis and acute inflammatory infiltration occur within the first 24 h following antibody injection, followed by the onset of mesangial cell proliferation and proteinuria at approximately 48 h, with peak pathological severity typically observed around day 5 [6]. Accordingly, treatment was initiated on day 2 post-induction to target the critical transition from the early inflammatory phase to the proliferative phase. Consecutive daily administrations on days 2, 3, and 4 were designed to maintain therapeutic exposure throughout the peak window of mesangial cell proliferation and matrix expansion, with efficacy evaluated on day 5 corresponding to maximal disease severity.

Rats were randomly assigned to six experimental groups (n = 5): Normal (healthy controls), PBS (disease model treated with PBS), free CLT, CLT-PLNs, CLT@R8-PLNs, and RES-blocking group (blank nanoparticles followed by CLT@R8-PLNs). All treatment groups received intravenous injections at an equivalent CLT dose of 1 mg/kg on days 2, 3, and 4 after model induction (Figure 4a).

Following OX-7 injection, pronounced proteinuria developed within 48 h, indicating successful establishment of renal injury and functional impairment characteristic of MsPGN [6]. Quantification of 24-h urinary protein excretion showed that all CLT-containing formulations significantly reduced proteinuria compared with the PBS-treated group. Notably, CLT@R8-PLNs and, in particular, the RES- blocking group achieved the greatest reduction in urinary protein levels (Figure 4b). Consistently, serum biochemical analysis revealed that the urea and creatinine levels were most effectively reduced in the RES-blocking group (Figure 4c and d), suggesting superior restoration of renal function.

Histopathological evaluation further substantiated these functional findings. H&E-stained kidney sections from the PBS-treated displayed severe pathological alterations, including glomerular atrophy, tubular vacuolar degeneration, tubular epithelial injury, and marked mesangial proliferation (Figure 4e). All treatment groups exhibited varying degrees of pathological improvement. Among them, CLT@R8-PLNs and specially the RES-blocking group demonstrated the most pronounced attenuation of renal injury. Kidneys from the RES-blocking group displayed markedly reduced glomerular swelling and only mild mesangial expansion, with overall glomerular architecture closely resembling that of healthy controls (Figure 4e). These observations indicate a superior capacity of this combined strategy to ameliorate glomerular injury and preserve renal morphology.

In MsPGN, activated mesangial cells secrete chemokines and adhesion molecules such as MCP-1 and ICAM-1, which promote monocyte/macrophage recruitment into the glomeruli [45, 46]. These infiltrating immune cells subsequently release pro-inflammatory cytokines, including IL-6 and IL-1β, thereby establishing a self-amplifying inflammatory-proliferative loop that drives disease progression47, 48. To determine whether CLT@R8-PLNs could interrupt this pathogenic cascade, the mRNA expression of MCP-1, ICAM-1, IL-6, and IL-1β in renal tissues was quantified by RT-PCR. Compared with healthy

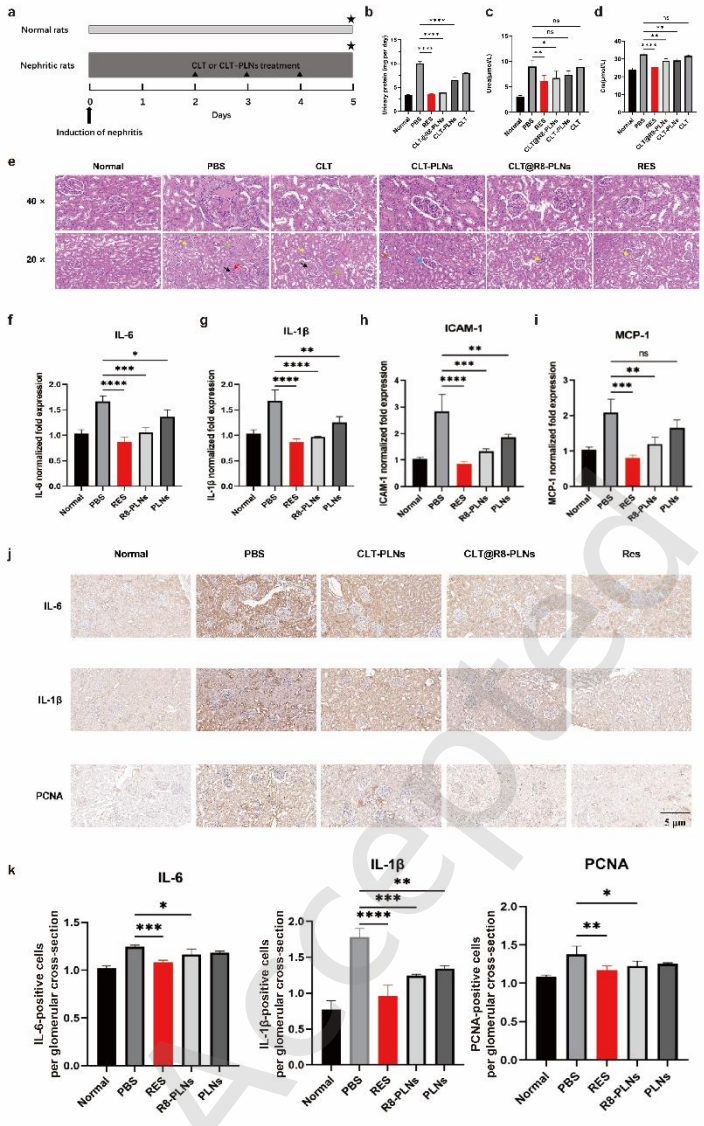

Fig. 4 | *In vivo* therapeutic efficacy of RES-blocking strategy in MsPGN rats. (a) Schematic diagram of treatment regimen. Solid triangles (▲) indicate I.V. administration of CLT formulations. Solid stars (★) denote concomitant nephrectomy and terminal sampling. (b) 24-h urinary protein excretion (n = 5), showing significant reduction in RES-blocking and CLT@R8-PLNs groups. (c, d) Serum Cre and Urea levels after treatment (n = 5), with notable reduction in RES- blocking group. (e) Representative H&E-stained kidney sections. RES-blocking groups demonstrated the most pronounced therapeutic benefits, with only mild mesangial hyperplasia. Arrows indicate pathological features: glomerular necrosis (black), inflammatory cell infiltration (red), mesangial hyperplasia (yellow), protein casts (green), glomerular atrophy (blue), and tubular vacuolar degeneration (orange). (f-i) Renal mRNA expression of IL-6, IL-1β, ICAM-1, and MCP-1 determined by PCR. The RES- blocking group showed the most pronounced downregulation. (j) Representative images of IL-6， IL-1β, and PCNA staining in glomeruli on day 5. RES-blocking group produced the strongest suppression of inflammatory and proliferative markers. Scale bar: 5 μm. (k) Quantification of IL-6， IL-1β, and PCNA expression. All data are presented as mean ± SD, *p< 0.05, ** p < 0.01, *** p < 0.001, **** p < 0.0001, vs. PBS model group, ns: not significant.

controls, all four markers were significantly upregulated in the PBS-treated model group, whereas treatment with CLT-containing formulations markedly suppressed their expression to varying extents. Notably, the RES- blocking group exhibited the most pronounced downregulation across all inflammatory markers (Figure 4f-i).

These transcriptional changes were further corroborated at the protein level by immunohistochemical analysis. Expression of IL-6 and IL-1β was attenuated in all treatment groups, with the strongest suppression observed in the RES- blocking group (Figure 4j and k). In parallel, staining for PCNA indicated that mesangial cell proliferation was most effectively inhibited in the RES- blocking group (Figure 4j and k). Together, these results demonstrate that CLT@R8-PLNs, particularly when administered following RES blockade, achieve efficient glomerular accumulation and exert potent anti-inflammatory and anti-proliferative effects. By simultaneously suppressing MCP- 1/ICAM- 1-mediated immune cell recruitment and IL- 6/IL- 1β-driven inflammatory amplification, this targeted nanotherapy effectively disrupts the vicious cycle of mesangial activation, providing a clear mechanistic basis for its therapeutic efficacy in MsPGN.

3.5 Preliminarily ensured systemic safety of the RES-blocking strategy

To preliminarily evaluate the systemic safety of the RES-blocking strategy, healthy SD rats were randomly assigned to five groups (n = 5 per group): Normal, free CLT, CLT-PLNs, CLT@R8-PLNs,

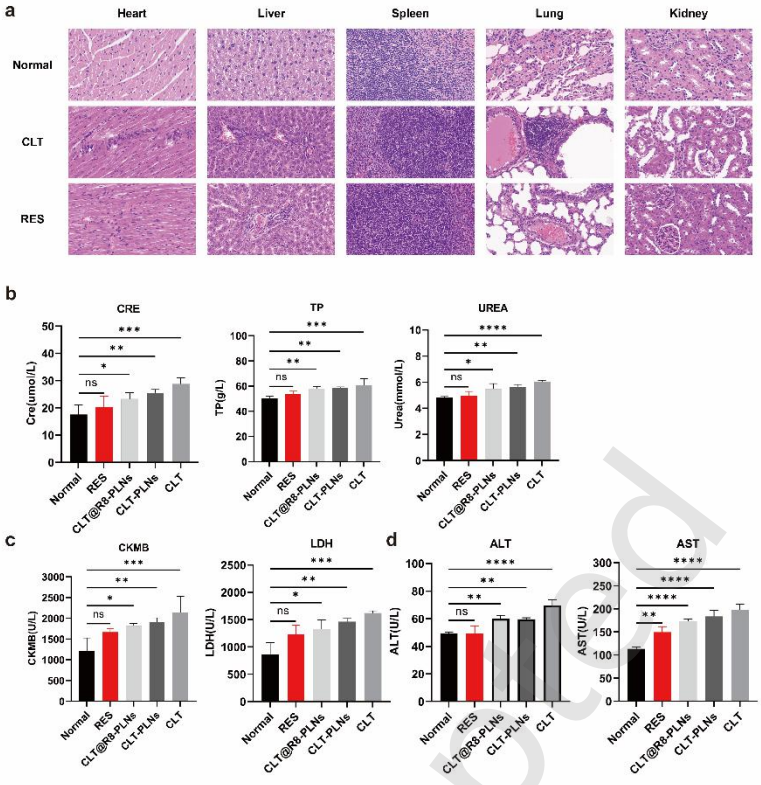

Fig. 5 | Evaluation of systemic toxicity following RES-blocking strategy. (a) H&E staining of heart, liver, spleen, lung and kidney from rats treated with free CLT or RES-blocking strategy. The RES- blocking group exhibited no obvious pathological alterations, whereas free CLT induced marked multi-organ toxicity. (b-d) Serum biochemical markers reflecting renal (CRE, UREA), hepatic (ALT, AST, TP), and cardiac (CKMB, LDH) function in different treatment groups. The RES- blocking strategy effectively mitigated CLT-associated multi- organ toxicity at an equivalent dose. All data are presented as mean ± SD, * p< 0.05, ** p < 0.01, *** p < 0.001, **** p < 0.0001, vs. Normal group, ns: not significant.

and RES-blocking group (rats pretreated with blank nanoparticles followed by CLT@R8-PLNs). All formulations were administered intravenously at an equivalent CLT dose of 1 mg/kg once daily for three consecutive days.

After the final administration, major organs including the heart, liver, spleen, lungs, and kidneys were harvested for histopathological examination by H&E staining. Compared with the Normal group, rats treated with free CLT exhibited pronounced histopathological abnormalities indicative of multi- organ toxicity (Figure 5A). In the lungs, free CLT induced marked inflammatory cell infiltration within the bronchial smooth muscle layer, peribronchial lymphoid follicle formation, epithelial necrosis and desquamation, accompanied by mild vascular wall hyperplasia and focal hemorrhage. Cardiac sections revealed myocardial fiber hypertrophy, atrophy, thinning, and fragmentation, together with nuclear degeneration, necrosis, fibroblast proliferation, inflammatory infiltration, and occasional hemorrhage. In the liver, extensive hepatocellular necrosis and inflammatory infiltration were observed, indicating significant liver injury. These findings are particularly notable given that CLT is known to exhibit dose-dependent systemic toxicity, with reported cardiotoxicity, hepatotoxicity, and pulmonary toxicity at therapeutic doses (1-5 mg/kg), which has limited its clinical application [15, 16, 49].

In contrast, animals in the RES- blocking group showed no overt pathological alterations in the examined organs, with tissue morphology comparable to that of the Normal group (Figure 5A). These findings indicate that, while free CLT at the therapeutic dose induces considerable pulmonary, cardiac, and hepatic toxicity, the RES- blocking nano- delivery strategy markedly alleviates these off- target adverse effects, thereby improving overall systemic tolerability.

Systemic safety was further assessed by analyzing serum biochemical markers reflecting the functional status of major organs. Renal function parameters (creatinine, CRE; urea nitrogen, UREA), hepatic enzymes (alanine aminotransferase, ALT; aspartate aminotransferase, AST; total protein, TP), and cardiac injury markers (creatine kinase-MB, CKMB; lactate dehydrogenase, LDH) were quantified. Analysis of renal function indicators showed that the RES blocking group did not exhibit significant renal dysfunction, whereas other treatment groups showed varying degrees of renal impairment (Figure 5B). Analysis of cardiac biomarkers demonstrated that CLT-induced cardiotoxicity was effectively mitigated in the RES blocking group, with CKMB and LDH levels comparable to those of healthy controls (Figure 5C). Similarly, hepatic function analysis revealed substantially in the RES-blocking group relative to free CLT and other formulations (Figure 5D).

The improved hepatic safety profile is likely attributable to the pre-saturation of hepatic Kupffer cells by blank nanoparticles, which reduces nonspecific hepatic uptake and limits direct exposure of CLT to liver [41, 42]. Collectively, these histopathological and biochemical results demonstrate that RES blockade significantly attenuates multi organ toxicity associated with free CLT at an equivalent therapeutic dose.

In this study, RES blockade was employed as a functional strategy to transiently reduce nanoparticle sequestration by phagocytic organs during the therapeutic window. It is noteworthy that transient RES saturation itself did not induce detectable toxicity in healthy animals, which is

consistent with previous reports demonstrating the reversibility and favorable safety profile of this strategy [32, 42, 50]. These findings support the feasibility of combining RES blockade and targeted nanotherapy to enhance the therapeutic window of CLT.

4 Conclusions

MsPGN is a progressive renal disorder that often progresses to ESRD, highlighting the urgent need for effective and kidney-targeted therapies. In this study, we developed a mechanistically guided delivery strategy that integrates cationic R8- mediated glomerular targeting with RES blockade to enhance renal delivery of CLT. By pre- administering blank PLGA nanoparticles (~200 nm) 1.5 h prior to the injection of CLT@R8- PLNs (~80 nm), the RES was temporarily saturated, resulting in prolonged systemic circulation and a pronounced redirection of a greater fraction of the therapeutic payload toward the kidneys. This RES- blocking approach substantially increased glomerular accumulation of CLT@R8- PLNs, resulting in pronounced therapeutic benefits in a rat anti- Thy1.1 MsPGN model. Specifically, the integrated strategy markedly reduced proteinuria, alleviated glomerular inflammation, and suppressed mesangial cell proliferation, accompanied by the downregulation of key pro-inflammatory mediators (IL- 6, IL- 1β, MCP- 1, and ICAM- 1) and the proliferation marker PCNA. While the anti-Thy1.1 model represents an acute and self- limiting form of MsPGN and may not fully capture the chronic and progressive nature of human disease, the key pathological features targeted in this study, such as mesangial cell proliferation and glomerular inflammation, are shared across both acute and chronic glomerulonephritis. The enhanced glomerular delivery achieved through RES blockade and R8-mediated targeting is therefore expected to be applicable to chronic settings, where sustained inflammation and altered glomerular microenvironments may further facilitate nanoparticle accumulation. Future studies using chronic kidney disease models will be valuable to confirm the translational potential of this therapeutic strategy. Notably, while free CLT administration induced evident multi- organ toxicity, RES blockade minimized off-target exposure and improved systemic safety without introducing additional pharmacological interventions.

Overall, These findings underscore the value of temporarily modulating host clearance pathways as a practical strategy to improve the therapeutic index of nanomedicines. RES blockade thus represents a broadly applicable approach for improving glomerular targeting and mitigate systemic toxicity, offering a promising framework for the delivery of potent yet toxicity-limited therapeutics in glomerulonephritis and other renal diseases.

Electronic Supplementary Material: Supplementary material (please provide the brief detail of the ESM) is available in the online version of this article at https://doi.org/10.26599/NR.2026.94908676.

Data availability

All data needed to support the conclusions in the paper are presented in the manuscript and/or the Electronic Supplementary Material. Additional data related to this paper may be requested from the corresponding author upon request.

Acknowledgements

We acknowledge the support from National Natural Science Foundation of China (No. 82273877), Natural Science Foundation of Zhejiang Province (LMS26H300004) and Natural Science Foundation of Hangzhou (2025SZRJJ1760).

Declaration of competing interest

All the contributing author(s) report(s) no conflict of interests in this work.

Author contribution statement

Q. Lin, Y. Wang and J. Fu conceived of the idea and designed the experiments; J. Fu, Y. Wang, A. Zhang, T. Li, Y. Yuan, K. Chen and S. He performed the experiments. Y. Wang, J. Fu, S. He, L. Li and L. Guo analyzed the data. Z. Zhang, L. Zhang, T. Gong, X. Sun provided suggestions and technical support on the research. J. Fu, Y. Wang and Q. Lin wrote the paper. All authors contributed to the general discussion.

Informed consent

Not applicable.

Ethics statement

The animal experiments were carried out following the guidelines of the Animal Ethics Committee of Sichuan University for the Care and Use of Laboratory Animals and were approved by the Committee on Ethical Use of Animals of Sichuan University (Ethical code: No. KS2020022, Chengdu, China).

Use of AI statement

None.

References

[1] Lv, J.-C.; Zhang, L.-X. Prevalence and Disease Burden of Chronic Kidney Disease. In Renal Fibrosis: Mechanisms and Therapies. B. C. Liu; H. Y. Lan; L. L. Lv, Eds., 2019; pp 3-15.

[2] Sun, A.; Pollock, C. A.; Huang, C. Mitochondria-targeting therapeutic strategies for chronic kidney disease. Biochem. Pharmacol. 2025, 231.

[3] Kovesdy, C. P. Epidemiology of chronic kidney disease: an update 2022. Kidney International Supplements 2022, 12, 7-11.

[4] Anders, H.-J.; Kitching, A. R.; Leung, N.; Romagnani, P. Glomerulonephritis: immunopathogenesis and immunotherapy. Nat. Rev. Immunol. 2023, 23, 453-471.

[5] Zhang, J.; Xie, M.; Xia, L.; Yu, T.; He, F.; Zhao, C.; Qiu, W.; Zhao, D.; Liu, Y.; Gong, Y.; Yao, C.; Liu, L.; Wang, Y. Sublytic C5b-9 Induces IL-23 and IL-36a Production by Glomerular Mesangial Cells via PCAF-Mediated KLF4 Acetylation in Rat Thy-1 Nephritis. J. Immunol. 2018, 201, 3184-3198.

[6] Guo, L.; Luo, S.; Du, Z.; Zhou, M.; Li, P.; Fu, Y.; Sun, X.; Huang, Y.; Zhang, Z. Targeted delivery of celastrol to mesangial cells is effective against mesangioproliferative glomerulonephritis. Nat. Commun. 2017, 8.

[7] Schöcklmann, H. O.; Lang, S.; Sterzel, R. B. Regulation of mesangial cell proliferation. Kidney Int. 1999, 56, 1199-1207.

[8] Levey, A. S.; Atkins, R.; Coresh, J.; Cohen, E. P.; Collins, A. J.; Eckardt, K. U.; Nahas, M. E.; Jaber, B. L.; Jadoul, M.; Levin, A.; Powe, N. R.; Rossert, J.; Wheeler, D. C.; Lameire, N.; Eknoyan, G. Chronic kidney disease as a global public health problem: Approaches and initiatives - a position statement from Kidney Disease Improving Global Outcomes. Kidney Int. 2007, 72, 247-259.

[9] McGrogan, A.; Franssen, C. F. M.; de Vries, C. S. The incidence of primary glomerulonephritis worldwide: a systematic review of the literature. Nephrol. Dial. Transplant. 2011, 26, 414-430.

[10] Harris, E.; Tiganescu, A.; Tubeuf, S.; Mackie, S. L. The Prediction and Monitoring of Toxicity Associated with Long-Term Systemic

Glucocorticoid Therapy. Curr. Rheumatol. Rep. 2015, 17.

[11] Wu, Q.; Wang, J.; Wang, Y.; Xiang, L.; Tan, Y.; Feng, J.; Zhang, Z.; Zhang, L. Targeted delivery of celastrol to glomerular endothelium and podocytes for chronic kidney disease treatment. Nano Research 2022, 15, 3556-3568.

[12] Sun, Y.; Wang, C.; Li, X.; Lu, J.; Wang, M. Recent advances in drug delivery of celastrol for enhancing efficiency and reducing the toxicity. Frontiers in Pharmacology 2024, 15.

[13] Li, R.; Li, Y.; Zhang, J.; Liu, Q.; Wu, T.; Zhou, J.; Huang, H.; Tang, Q.; Huang, C.; Huang, Y.; Zhang, Z.; Zhang, G.; Zhao, Y.; Ma, L.; Feng, Y.; Mo, L.; Han, M.; He, J. Targeted delivery of celastrol to renal interstitial myofibroblasts using fibronectin-binding liposomes attenuates renal fibrosis and reduces systemic toxicity. Journal of Controlled Release 2020, 320, 32-44.

[14] Wang, S.; Liu, K.; Wang, X.; He, Q.; Chen, X. Toxic effects of celastrol on embryonic development of zebrafish. Drug Chem. Toxicol. 2011, 34, 61-65.

[15] Huang, Y.; Zhou, D.; Hang, T.; Wu, Z.; Liu, J.; Xu, Q.; Xie, X.; Zuo, J.; Wang, Z.; Zhou, Y. Preparation, characterization, and assessment of the antiglioma effects of liposomal celastrol. Anti-Cancer Drugs 2012, 23, 515-524.

[16] Yang, H.; Chen, D.; Cui, Q. C.; Yuan, X.; Dou, Q. P. Celastrol, a triterpene extracted from the Chinese "Thunder of God Vine," is a potent proteasome inhibitor and suppresses human prostate cancer growth in nude mice. Cancer Res. 2006, 66, 4758-4765.

[17] Gagliardi, M. Biomimetic and bioinspired nanoparticles for targeted drug delivery. Therapeutic delivery 2017, 8, 289-299.

[18] Omidian, H.; Wilson, R. L.; Castejon, A. M. Recent Advances in Peptide-Loaded PLGA Nanocarriers for Drug Delivery and Regenerative Medicine. Pharmaceuticals 2025, 18.

[19] Essa, D.; Kondiah, P. P. D.; Choonara, Y. E.; Pillay, V. The Design of Poly(lactide-co-glycolide) Nanocarriers for Medical Applications. Frontiers in Bioengineering and Biotechnology 2020, 8.

[20] Roointan, A.; Xu, R.; Corrie, S.; Hagemeyer, C. E.; Alt, K. Nanotherapeutics in Kidney Disease. J. Am. Soc. Nephrol. 2025, 36, 500-518.

[21] Choi, C. H. J.; Zuckerman, J. E.; Webster, P.; Davis, M. E. Targeting kidney mesangium by nanoparticles of defined size. Proc. Natl. Acad. Sci. U. S. A. 2011, 108, 6656-6661.

[22] Huang, Y.; Wang, J.; Jiang, K.; Chung, E. J. Improving kidney targeting: The influence of nanoparticle physicochemical properties on kidney interactions. Journal of Controlled Release 2021, 334, 127-137.

[23] Choubey, R.; Chatterjee, M.; Pandey, P. K.; Mishra, A.; Datta, B. Coassembly of Cell-Penetrating Peptide Octaarginine with Acetazolamide: Emergent Interactions with E. coli. Acs Omega 2024, 9, 46204-46216.

[24] Khalil, K. A.; Kogure, K.; Futaki, S.; Harashima, H. Octaarginine-modified liposomes: Enhanced cellular uptake and controlled intracellular trafficking. Int. J. Pharm. 2008, 354, 39-48.

[25] Singh, T.; Kang, D. H.; Kim, T. W.; Kong, H. J.; Ryu, J. S.; Jeon, S.; Ahn, T. S.; Jeong, D.; Baek, M. J.; Im, J. Intracellular delivery of oxaliplatin conjugate via cell penetrating peptide for the treatment of colorectal carcinoma in vitro and in vivo. Int. J. Pharm. 2021, 606.

[26] Liu, Y.; Ran, R.; Chen, J.; Kuang, Q.; Tang, J.; Mei, L.; Zhang, Q.; Gao, H.; Zhang, Z.; He, Q. Paclitaxel loaded liposomes decorated with a multifunctional tandem peptide for glioma targeting. Biomaterials 2014, 35, 4835-4847.

[27] Zhang, X.; Wang, H.; Coulter, J. A.; Yang, R. Octaarginine-modified gold nanoparticles enhance the radiosensitivity of human colorectal cancer cell line LS180 to megavoltage radiation. Int. J. Nanomedicine 2018, 13, 3541-3552.

[28] Wilhelm, S.; Tavares, A. J.; Dai, Q.; Ohta, S.; Audet, J.; Dvorak, H. F.; Chan, W. C. W. Analysis of nanoparticle delivery to tumours. Nature Reviews Materials 2016, 1.

[29] Cheng, Y.-H.; He, C.; Riviere, J. E.; Monteiro-Riviere, N. A.; Lin, Z. Meta-Analysis of Nanoparticle Delivery to Tumors Using a Physiologically Based Pharmacokinetic Modeling and Simulation Approach. ACS Nano 2020, 14, 3075-3095.

[30] Li, Z.; Zhu, Y.; Zeng, H.; Wang, C.; Xu, C.; Wang, Q.; Wang, H.; Li, S.; Chen, J.; Xiao, C.; Yang, X.; Li, Z. Mechano-boosting nanomedicine antitumour efficacy by blocking the reticuloendothelial system with stiff nanogels. Nat. Commun. 2023, 14.

[31] Zhang, Y.-N.; Poon, W.; Tavares, A. J.; McGilvray, I. D.; Chan, W. C. W. Nanoparticle-liver interactions: Cellular uptake and hepatobiliary elimination. Journal of Controlled Release 2016, 240, 332-348.

[32] Sun, X.; Yan, X.; Jacobson, O.; Sun, W.; Wang, Z.; Tong, X.; Xia, Y.; Ling, D.; Chen, X. Improved Tumor Uptake by Optimizing Liposome Based RES Blockade Strategy. Theranostics 2017, 7, 319-328.

[33] Tang, Y.; Wang, X.; Li, J.; Nie, Y.; Liao, G.; Yu, Y.; Li, C. Overcoming the Reticuloendothelial System Barrier to Drug Delivery with a "Don't-Eat-Us" Strategy. ACS Nano 2019, 13, 13015-13026.

[34] Yu, C.; Zhou, Q.; Xiao, F.; Li, Y.; Hu, H.; Wan, Y.; Li, Z.; Yang, X. Enhancing Doxorubicin Delivery toward Tumor by Hydroxyethyl Starch-g-Polylactide Partner Nanocarriers. ACS Appl. Mater. Interfaces 2017, 9, 10481-10493.

[35] Wu, J.; Zheng, Y.; Liu, M.; Shan, W.; Zhang, Z.; Huang, Y. Biomimetic Viruslike and Charge Reversible Nanoparticles to Sequentially Overcome Mucus and Epithelial Barriers for Oral Insulin Delivery. ACS Appl. Mater. Interfaces 2018, 10, 9916-9928.

[36] Wan, Y.; Sun, W.; Che, X.; Yang, H.; Ge, M.; Dai, W.; Shimizu, F. Suppressive effects of GTW treatment on infiltration of inflammatory cell in glomeruli in anti-Thy1.1 glomerulonephritis. China journal of Chinese materia medica 2009, 34, 72-77.

[37] Ogawa, K.; Ishii, Y.; Toyoda, T. Role and potential of histopathological specimens in the toxicological evaluation of pharmaceuticals and chemicals. Nihon yakurigaku zasshi. Folia pharmacologica Japonica 2022, 157, 139-145.

[38] Xu, Y.; Kim, C.-S.; Saylor, D. M.; Koo, D. Polymer degradation and drug delivery in PLGA-based drug-polymer applications: A review of experiments and theories. Journal of Biomedical Materials Research Part B-Applied Biomaterials 2017, 105, 1692-1716.

[39] Rahmani, F.; Naderpour, S.; Nejad, B. G.; Rahimzadegan, M.; Ebrahimi, Z. N.; Kamali, H.; Nosrati, R. The recent insight in the release of anticancer drug loaded into PLGA microspheres. Med. Oncol. 2023, 40.

[40] Yoo, J.; Won, Y.-Y. Phenomenology of the Initial Burst Release of Drugs from PLGA Microparticles. Acs Biomaterials Science & Engineering 2020, 6, 6053-6062.

[41] Delledonne, A.; Morla-Folch, J.; Anzola, M.; Bertocchi, F.; Vargas-Nadal, G.; Kober, M.; Sissa, C.; Ventosa, N.; Painelli, A. Increasing resonance energy transfer upon dilution: a counterintuitive observation in CTAB micelles. Journal of Materials Chemistry C 2021, 9, 10952-10964.

[42] Liu, F.; Han, L.; Huang, X.; Sang, M.; Liu, B.; Li, C.; Ma, C.; Liu, W.; Feng, F.; Qu, W. Reticuloendothelial System Pre-Block Strategy to Improve Tumor Targeting Efficacy for Hyaluronic Acid Related Drug Delivery System. J. Biomed. Nanotechnol. 2018, 14, 1731-1743.

[43] Yu, M.; Zheng, J. Clearance Pathways and Tumor Targeting of Imaging Nanoparticles. ACS Nano 2015, 9, 6655-6674.

[44] Gao, H.; Wang, Y.; Fu, J.; Yuan, Y.; Li, T.;Zhang, A.; He, W.; He, S.; Huang, S.; Li, L.; Qu, M.; Guo, L.; Sun, X.; Gong, T.; Zhang, L.; Lin, Q.; Zhang, Z. Monocyte Membrane-Fused Liposomes for Enhanced Targeted Treatment of Mesangioproliferative Glomerulonephritis. ACS Appl. Mater. Interfaces 2025, 17, 67641-67654.

[45] Kawasaki, K.; Yaoita, E.; Yamamoto, T.; Tamatani, T.; Miyasaka, M.; Kihara, I. ANTIBODIES AGAINST INTERCELLULAR-ADHESION MOLECULE-1 AND LYMPHOCYTE FUNCTION-ASSOCIATED ANTIGEN-1 PREVENT GLOMERULAR INJURY IN RAT EXPERIMENTAL CRESCENTIC GLOMERULONEPHRITIS. J. Immunol. 1993, 150, 1074-1083.

[46] Wenzel, U.; Schneider, A.; Valente, A. J.; Abboud, H. E.; Thaiss, F.; Helmchen, U. M.; Stahl, R. A. K. Monocyte chemoattractant protein-1 mediates monocyte/macrophage influx in anti-thymocyte antibody-induced glomerulonephritis. Kidney Int. 1997, 51, 770-776.

[47] Horii, Y.; Iwano, M.; Hirata, E.; Shiiki, H.; Fujii, Y.; Dohi, K.;

Ishikawa, H. ROLE OF INTERLEUKIN-6 IN THE PROGRESSION OF MESANGIAL PROLIFERATIVE GLOMERULONEPHRITIS. Kidney Int. 1993, 43, S71-S75.

[48] Tesch, G. H.; Lan, H. Y.; Atkins, R. C.; NikolicPaterson, D. J. Role of interleukin-1 in mesangial cell proliferation and matrix deposition in experimental mesangioproliferative nephritis. Am. J. Pathol. 1997, 151, 141-150.

[49] Wagh, P. R.; Desai, P.; Prabhu, S.; Wang, J. Nanotechnology-Based Celastrol Formulations and Their Therapeutic Applications. Frontiers in Pharmacology 2021, 12.

[50] Makadia, H. K.; Siegel, S. J. Poly Lactic-co-Glycolic Acid (PLGA) as Biodegradable Controlled Drug Delivery Carrier. Polymers 2011, 3, 1377-1397.

Electronic Supplementary Material

Reticuloendothelial system blockade-assisted redirection of celastrol-loaded nanomedicine to glomeruli for treatment of mesangioproliferative glomerulonephritis.

Jiali Fu[1,§], Yujia Wang[1,§], Anqi Zhang[1], Ting Li[1], Yan Yuan[1], Kejin Chen[1], Shanshan He[2], Lin Li[3], Shiqi Huang[4], Ling Guo[5], Xun Sun[1], Tao Gong[1], Ling Zhang[3,4], Qing Lin[1] ✉, and Zhirong Zhang[1]

[1] *Key Laboratory of Drug Targeting and Drug Delivery System of the Education Ministry and Sichuan Province, Sichuan Engineering Laboratory for Plant-Sourced Drug and Sichuan Research Center for Drug Precision Industrial Technology, West China School of Pharmacy, Sichuan University, Chengdu 610041, China*

[2] *College of Pharmaceutical Sciences, Liangzhu Laboratory, Zhejiang University, Hangzhou 310058, China*

[3] *West China School of Public Health and West China Fourth Hospital, Sichuan University, Chengdu 610041, China*

[4] *College of Polymer Science and Engineering, Sichuan University, Chengdu 610065, China*

[5] *National Engineering Technology Research Center for Miao Medicine, Guizhou Engineering Technology Research Center for Processing and Preparation of Traditional Chinese Medicine and Ethnic Medicine, College of Pharmaceutical Sciences, Guizhou University of Traditional Chinese Medicine, Guiyang 550025, China*

[§] *Jiali Fu and Yujia Wang contributed equally to this work.*

✉ Address correspondence to qinglin@scu.edu.cn

Supporting information to https://doi.org/10.26599/NR.2026.94908676

Table S1. Effect of polymer concentration on the formulation properties of R8-PLNs

Polymer concentration (mg/mL)	Size (nm)	PDI
0.5	82.37	0.197
1	95.00	0.205
1.5	135.00	0.212
2	189.56	0.234

Table S2. Impact of R8 concentration on the zeta potential of PLGA Nanoparticles

PEG2000: R8	Zeta (mV)
0	-22.24
2:1	+11.1
1:1	+22.68
1:2	+36.43

Table S3. Impact of agitation time on the PDI of R8-PLNs

Agitation time (min)	Size (nm)	PDI
10	97.24	0.357
20	95.15	0.312
30	82.28	0.178
40	85.54	0.131

Table S4. Impact of speed on the property of R8-PLNs

Agitation speed (rpm)	Size (nm)	PDI
900	122.2	0.298
1000	111.95	0.256
1100	108.16	0.134
1200	89.46	0.131

Table S5. The particle size, PDI and zeta potential of CLT@R8-PLNs

Size (nm)	PDI	Zeta potential (mV)
74.92±0 .94	0.205±0.013	13.63±0.72

Table S6. The particle size、PDI and zeta potential of CLT@R8-PLNs

EE%	DL%
94.02±0.75%	2.58±0.04%

Table S7. The particle size and PDI of blank PLGA nanoparticles

Size (nm)	PDI
200.87 ± 2.64 nm	0.185±0.025